

PAPER

## First-principles calculations and Raman scattering evidence for local symmetry lowering in rhombohedral ilmenite: temperature- and pressure-dependent studies

To cite this article: J E Rodrigues *et al* 2018 *J. Phys.: Condens. Matter* **30** 485401

View the [article online](#) for updates and enhancements.



**IOP | ebooks**<sup>TM</sup>

Bringing you innovative digital publishing with leading voices to create your essential collection of books in STEM research.

Start exploring the collection - download the first chapter of every title for free.

# First-principles calculations and Raman scattering evidence for local symmetry lowering in rhombohedral ilmenite: temperature- and pressure-dependent studies

J E Rodrigues<sup>1,4,5</sup>, M M Ferrer<sup>2</sup>, T R Cunha<sup>1</sup>, R C Costa<sup>3</sup>,  
J R Sambrano<sup>2</sup>, A D Rodrigues<sup>1</sup> and P S Pizani<sup>1</sup>

<sup>1</sup> Optical Spectroscopy and Raman Scattering Research Group, Federal University of São Carlos, São Carlos SP 13565-905, Brazil

<sup>2</sup> Modeling and Molecular Simulations Research Group, São Paulo State University, UNESP, Bauru SP 17033-360, Brazil

<sup>3</sup> Department of Environmental Engineering, Federal University of Campina Grande, Pombal PB 58840-000, Brazil

E-mail: [rodrigues.joaobelias@gmail.com](mailto:rodrigues.joaobelias@gmail.com) and [rodrigues.joaobelias@df.ufscar.br](mailto:rodrigues.joaobelias@df.ufscar.br)

Received 25 August 2018, revised 28 September 2018

Accepted for publication 12 October 2018

Published 7 November 2018




CrossMark

## Abstract

ATiO<sub>3</sub>-type materials may exist in two different crystalline forms: the perovskite and ilmenite. While many papers have devoted their attention to evaluating the structural properties of the perovskite phase, the structural stability of the ilmenite one still remains unsolved. Here, we present our results based on the lattice dynamics and first-principles calculations (density functional theory) of the CdTiO<sub>3</sub> ilmenite phase, which are confronted with experimental data obtained through micro Raman spectroscopy that is a very good tool to probe the local crystal structure. Additional Raman bands, which are not foreseen from group-theory for the ilmenite rhombohedral structure, appeared in both low temperature (under vacuum condition) and high-pressure (at room temperature) spectra. The behavior can be explained by considering the local loss of inversion symmetry operation which reduces the overall space group from  $R\bar{3}$  ( $C_{3i}^2$ ) to  $R3$  ( $C_3^4$ ). Our results can also be extended to other ilmenite-type compositions.

Keywords: ilmenite, Raman spectroscopy, factor group analysis, inversion operation, CdTiO<sub>3</sub>, density functional theory

 Supplementary material for this article is available [online](#)

(Some figures may appear in colour only in the online journal)

## 1. Introduction

There is no doubt that ABX<sub>3</sub> perovskites are a key material for developing new devices for several applications, covering the fields of gas sensors [1], detectors [2], solar cells [3], actuators

[4], capacitors [5], microwave resonators [6], ferroelectric random access memory [7], superconductors [8], waveguides [9], catalysts [10], and so on [11–14]. Such practical uses are possible due to their ability to accommodate very different atoms at both A- and B-sites that generates complex systems with tunable physical properties [10]. In ideal cubic perovskite, the B atoms are octahedrally coordinated by X

<sup>4</sup> Author to whom any correspondence should be addressed.

<sup>5</sup> <http://df.ufscar.br/>

anions (six-fold) to form a lattice of corner-sharing  $BX_6$  octahedra, while A atoms are centered at the 12 coordinate cavities (12-fold) generated by the octahedral arrangement [15]. A particular class of perovskites takes place when B-sites are populated by titanium atoms, including the well-known barium titanate for supercapacitor applications [16], strontium titanate for tunable microwave filters, and lead zirconate titanate for piezoelectric actuators [17]. All the interesting properties of these materials come from the atomic substitution-driven crystal structure in which its description is ruled by three processes, namely octahedral tilting, off-center cationic displacement or octahedral distortion [18]. In this way, the ideal perovskite modifies its crystal structure to a less symmetric space group which makes possible monitor the phase transition through soft modes studies [19, 20].

In  $ATiO_3$  titanates, A site may lead to a strong distorted structure when Fe, Mn, Zn, Ni, Co, Cd or Mg-type atoms are considered, and hence the corner-sharing  $TiO_6$  network is no long valid [21]. Instead, an ordered corundum-type lattice takes place to describe such a new class of titanates, known as ilmenites. In particular, the octahedral network is appropriated understood as ordered layers of edge-sharing  $AO_6$  and  $TiO_6$  octahedra following the 1:1 stacking sequence along  $[1\ 1\ 1]_R$  planes of the rhombohedral unit cell (i.e. parallel to  $c$ -axis in hexagonal description). The reduced size of A atoms allows coordination number variation from 12 to 6 in ilmenite materials, as compared to ideal perovskite, and then a symmetry lowering [22]. Similar to perovskites, ilmenite-based oxides also find innumerable applications in heterogeneous catalysis [23], gas sensing [24], sodium ion battery technology [25], and high- $k$  dielectrics [26], being the thermodynamic stability the main hindrance for their widespread use in novel devices.

A particular and representative of the  $ATiO_3$ -type compound is the cadmium titanate ( $CdTiO_3$ ) that can be synthesized in either perovskite or ilmenite crystal forms (polymorphism), making it an appropriated laboratory for high studies in solid state physics.  $CdTiO_3$  perovskite is paraelectric at room temperature belonging to the orthorhombic  $Pnma$  space group ( $D_{2h}^{16}$  or #62) [27, 28]. Below  $\sim 80$  K, such a phase undergoes a displacive ferroelectric transition to a polar orthorhombic phase within the  $Pna2_1$  space group ( $C_{2v}^9$  or #33) that is an interesting combination of octahedral tilting, from the overall centrosymmetric orthorhombic phase, and cationic displacement of Ti and O ions [29]. Otherwise,  $CdTiO_3$  in ilmenite phase (here after: II-type  $CdTiO_3$ ) is structurally stable under ambient pressure and at temperatures below 1173 K. Until now, important papers were published concerning structural, vibrational and elasticity properties of  $CdTiO_3$  polymorphs [30–34]. Such studies investigated the phase diagram concerning the ilmenite  $\rightarrow$  perovskite transition. Although the temperature stability of the II-type  $CdTiO_3$  is well-known, there are no available reports on the hydrostatic pressure stability by means of Raman scattering which makes this issue a hot topic for solid state community.

In this work, we have done temperature- and pressure-dependent experimental investigations using micro Raman spectroscopy to better characterize the lattice dynamics of the  $CdTiO_3$  ilmenite. Theoretical calculations using group-theory,

density functional theory, and short-range force field model were performed to provide the correct symmetry assignments of the optical modes in II-type  $CdTiO_3$ . Our theoretical lattice model was compared with the experimental results in order to explain the occurrence of extra Raman modes at low temperature (under vacuum condition) and under high-pressure (at ambient temperature). The results allow us to suggest a local reduction in crystal symmetry based on the break of inversion operation which leads to unexpected modes in the experimental Raman spectra.

## 2. Experimental procedures

### 2.1. Synthesis

Fine powders of II-type  $CdTiO_3$  were prepared by the conventional solid state reaction method, starting from CdO (Sigma-Aldrich; 99.9%) and  $TiO_2$  (Sigma-Aldrich; 99.9%) oxides. These reactants were weighted and mixed for 1 h by high-energy vibratory milling using deionized water as a mixing medium. The dry mixture was thermally treated in air at 1023 K for 2 h and then ground into fine powder with an agate mortar and pestle.

### 2.2. Characterization

Conventional x-ray diffraction (XRD) at room conditions was carried out in a 6100 Shimadzu diffractometer (40 kV and 30 mA; Cu- $K_\alpha$  radiation with  $\lambda = 1.5406$  Å) over a  $2\theta$  interval between  $20^\circ$  and  $80^\circ$  with a step size of  $0.02^\circ$ . The XRD pattern was compared with card N° 262708 [27] available at the inorganic crystal structure database (ICSD, FIZ Karlsruhe, and NIST). Rietveld refinement was performed using the *DBWS9807* free software [35, 36]. Raman spectra were recorded in a HR800 Evolution micro Raman spectrometer (Horiba *Jobin-Yvon*) equipped with a Peltier-cooled CCD camera and a holographic diffraction grating of  $1800\text{ gr mm}^{-1}$  in order to keep the spectral resolution better than  $\sim 1\text{ cm}^{-1}$ . The Stokes signals were excited by a 488 nm laser line through a  $50\times$  LD objective ( $NA = 0.35$  and spot size  $\sim 1\ \mu\text{m}$ ) and the laser power was kept below  $\sim 3\text{ mW}$ .

For the temperature-dependent Raman studies under ambient pressure, a small amount of sample was placed in a helium closed cycle cryostat with a controller Lake Shore 330 and in a Linkan T1500 micro furnace during low- and high-temperature studies, respectively, covering the interval between 15 and 1173 K. All the spectra were further corrected by the Bose–Einstein thermal factor before any fitting procedure in the framework of the PeakFit v.4 software [37]. Besides, Lorentzian profile curves were used to decompose the spectra into component peaks from which it was extracted both width and position parameters. For the pressure-dependent Raman studies at ambient temperature, small sample amount was placed in a symmetric piston cylinder-type diamond anvil cell equipped with  $400\ \mu\text{m}$  diamond culets. First, the stainless steel gasket was pre-indented to  $30\ \mu\text{m}$  in thickness and then a bore with  $100\ \mu\text{m}$  of diameter was drilled. After,  $CdTiO_3$  grains together with ruby microspheres, which was employed as a

pressure sensor [38, 39], were carefully loaded between two opposing diamonds anvils (see online supplementary figure S1 ([stacks.iop.org/JPhysCM/30/485401/mmedia](http://stacks.iop.org/JPhysCM/30/485401/mmedia))). Finally, the 16:4:1 methanol-ethanol-water mixture was filled in the pressure chamber as a pressure transmitting medium (PTM) from ~0 up to 18.5 GPa.

### 3. Theoretical procedures

#### 3.1. Quantum computational methods

Quantum computational simulations were performed by periodic functional theory (DFT) in conjunction with B3LYP hybrid functional implemented [40, 41] on *CRYSTAL17* program [42]. Cadmium, titanium, and oxygen centers were described by POB\_TZVP [43], 8-6411(31d)G [44] and 8-411(1d)G [44] basis sets, respectively. The calculations were conducted with truncation criteria for the Coulomb and exchange series controlled by a set of five thresholds ( $10^{-8}$ ,  $10^{-8}$ ,  $10^{-8}$ ,  $10^{-8}$ , and  $10^{-16}$ ), and shrinking factors set to 8 and 8 (Pack-Monkhorst and Gilat net). The initial atomic positions and lattice parameters were set according to Rietveld refinement results. The Raman and infrared vibrational modes and their corresponding wavenumbers were calculated by means of numerical second derivatives of the total energy. The Raman and infrared intensities were obtained by the CPHF/KS scheme [45, 46]. Hydrostatic pressures from 2 up to 18 GPa were applied by means of the stress tensor, as implemented in the *CRYSTAL* code.

#### 3.2. Classical computational methods

The optical modes of Il-type  $\text{CdTiO}_3$  were also described using the normal coordinate analysis in a context of the short-range force field model. In particular, we have taken as force constants the stretching ( $K_i$  and  $F_i$ ) and bending ( $H_i$ )-type ones in light of the first-neighbor approximation, as quoted in table 1. It is noteworthy that the bending forces are included to describe the transverse lattice vibrations [47]. Each force constant was then adjusted by least-square fitting. In this way, stretching interactions represent the forces between Cd–O, Ti–O, and O–O, while bending forces concern the angle bonds O–Cd–O and O–Ti–O. In this calculation, all the structural data including atomic positions, bond distances, and angles were extracted from the Rietveld refinement results.

The lattice dynamics calculations (LDC) were then performed in the framework of the Wilson's *GF*-matrix by solving the secular equation  $|\mathbf{F} - \lambda\mathbf{G}^{-1}| = 0$  [48]. Details on the classical theory of the molecular vibration are summarized in the seminal work of Wilson, Decius and Cross [49].  $\mathbf{G}$  and  $\mathbf{F}$  matrices contain the kinetic and potential energy data of the system, respectively. In short, the normal coordinates  $|\mathbf{Q}\rangle$  should be derived from internal coordinates  $|\mathbf{S}\rangle$  via  $\mathbf{L}$  matrix,  $|\mathbf{S}\rangle = \mathbf{L}|\mathbf{Q}\rangle$ , and then leading a diagonal matrix with the eigenvalues  $\lambda = 4\pi^2c^2\nu^2$ . Such a calculation also provides the percentage contribution of each force constant to an arbitrary

eigenvalue  $\lambda_k$  by the potential energy distribution (PED) coefficient, as follows:

$$\text{PED}_{ij}^k = \frac{F_{ij}L_{ik}L_{jk}}{\sum_{ij} F_{ij}L_{ik}L_{jk}}. \quad (1)$$

## 4. Results and discussion

#### 4.1. Crystal structure and Raman activity

Figure 1(a) exhibits the XRD pattern and its refinement at room temperature for the Il-type  $\text{CdTiO}_3$  sample. No signals of secondary phases were observed in this pattern, confirming that the stoichiometric  $\text{CdTiO}_3$  was fully obtained from CdO and  $\text{TiO}_2$  reactants. The reflection planes were indexed in agreement with the rhombohedral structure belonging to the  $R\bar{3}$  space group ( $C_{3i}^2$  or #148) to describe the ilmenite system, as reported in the ICSD card N° 262708 [27]. In the inset of figure 1(a), a representation of this rhombohedral unit cell containing two chemical formulas ( $Z = 2$ ) is also shown. From the structural refinement, the lattice parameters, unit cell volume, and atomic positions were obtained, as listed in table 2, in a good agreement with other reported data for the Il-type  $\text{CdTiO}_3$  [50, 51]. For comparison, the structural data predicted through DFT calculations is also quoted.

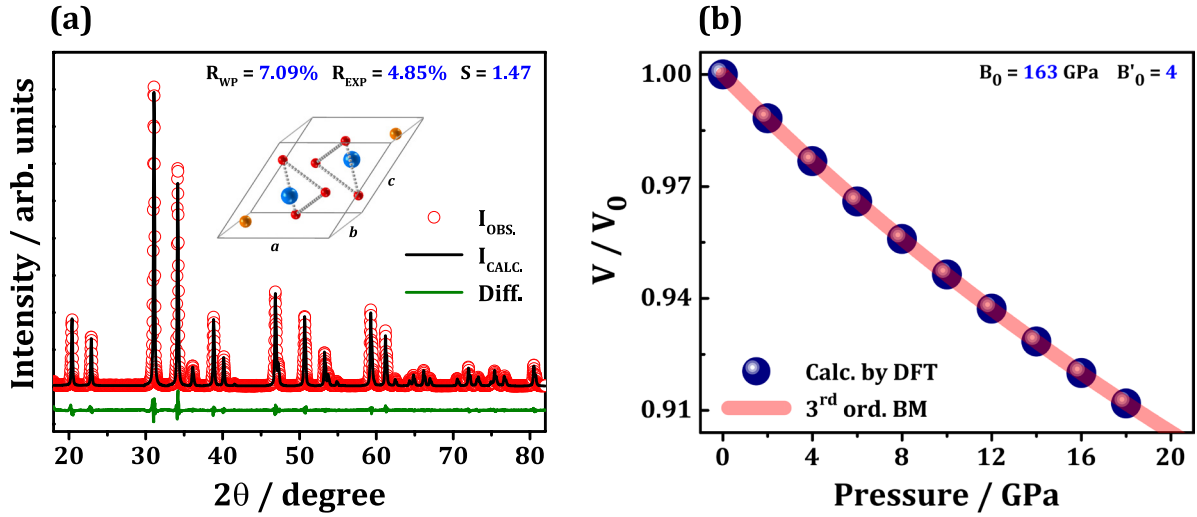
Since the present study also concerns the evolution of the lattice properties under high-pressure condition, the compressibility data for the Il-type  $\text{CdTiO}_3$  were predicted using DFT calculations. The stability of the rhombohedral unit cell was probed for pressure varying from 0 to 18 GPa. Figure 1(b) shows the pressure dependence of the unit cell volume ( $V$ ) normalized at its value at ambient condition  $V_0$  (volume at 0 GPa). The dimensions of the unit cell decreased as the pressure increased from 0 up to 18 GPa. The resistance to this compression can be evaluated by the Bulk modulus ( $B_0$ ) and its pressure derivative ( $B'_0 = \partial B_0 / \partial P$ ), being such parameters directly determined from the third-order Birch–Murnaghan isothermal equation of state, as follows [52]:

$$P(V) = \frac{3}{2}B_0 \left[ \left( \frac{V}{V_0} \right)^{-7/3} - \left( \frac{V}{V_0} \right)^{-5/3} \right] \left\{ 1 + \frac{3}{4}(B'_0 - 4) \left[ \left( \frac{V}{V_0} \right)^{-2/3} - 1 \right] \right\}, \quad (2)$$

where  $B_0 = 163$  GPa and  $B'_0 \lesssim 4$  were extracted from the fitting process, as shown in figure 1(b). These values are in relatively good agreement with other experimental and theoretical results already reported for the ilmenite-based compounds, such as  $\text{CdTiO}_3$  ( $B_0 = 165$  GPa) [30],  $\text{FeTiO}_3$  ( $B_0 = 172$  GPa) [53],  $\text{MnTiO}_3$  ( $B_0 = 176$  GPa) [54],  $\text{ZnTiO}_3$  ( $B_0 = 191$  GPa) [55], and  $\text{NiTiO}_3$  ( $B_0 = 195$  GPa) [56]. We can further conclude that the theoretical model developed here is suitable for describing the structural properties of Il-type  $\text{CdTiO}_3$  under high-pressure condition, and for elucidating the stability of the ilmenite phase in the pressure range 0–18 GPa.

**Table 1.** Multiplicity, interatomic distance or angle, and force constant values used to parameterize the potential energy matrix in the framework of the short-range force field model (SRFFM).

Force constant	Between atoms	Multiplicity	Distance (Å)/angle (°)	Force constant value (mdyn. Å <sup>-1</sup> )
Bonds				
$K_1$	Cd(2c)–O(6f)	6	2.219–2.424	0.801
$K_2$	Ti(2c)–O(6f)	6	1.887–2.062	0.826
$F_1$	O(6f)–O(6f)	3	2.500–2.737	0.534
Angles				
$H_1$	O(6f)–Cd(2c)–O(6f)	3	155.05	0.512
$H_2$	O(6f)–Ti(2c)–O(6f)	3	161.32	0.782

**Figure 1.** (a) X-ray powder diffraction data for Il-type CdTiO<sub>3</sub> at ambient condition. Red open circles indicate the experimental XRD data, the black line the Rietveld refined data, and the green line the difference between the measured and refined data. The inset exhibits the unit cell, with two formulas per unit, of the CdTiO<sub>3</sub> ilmenite. The orange, blue, and red spheres denote cadmium, titanium, and oxygen atoms, respectively. (b) Calculated pressure dependence of unit cell volume for Il-type CdTiO<sub>3</sub>. The thick red line is the fitted curve using the third-order Birch–Murnaghan isothermal equation of state.**Table 2.** Nuclear site group analysis for the Il-type CdTiO<sub>3</sub> with rhombohedral unit cell belonging to the  $R\bar{3}$  ( $C_{3i}^2$  or #148) space group. The atomic position and its site symmetry are also listed together with structural information extracted from Rietveld method and DFT calculation.

Atom	Wyckoff site	Symmetry	$x$	$y$	$z$	Irreducible representation
Cd <sub>1</sub>	2c	3. ( $C_3$ )	0.3640	0.3640	0.3640	$A_g \oplus A_u \oplus E_g \oplus E_u$
Ti <sub>1</sub>	2c	3. ( $C_3$ )	0.1503	0.1503	0.1503	$A_g \oplus A_u \oplus E_g \oplus E_u$
O <sub>1</sub>	6f	1 ( $C_1$ )	0.5652	−0.0367	0.1912	$3A_g \oplus 3A_u \oplus 3E_g \oplus 3E_u$
Unit cell data		Rietveld	DFT		$\Gamma_{TOTAL}$	$5A_g \oplus 5A_u \oplus 5E_g \oplus 5E_u$
Cell parameter, $a$ (Å)		5.7964	5.8690		$\Gamma_{ACOUSTIC}$	$A_u \oplus E_u$
Cell parameter, $\alpha$ (°)		53.72	53.61		$\Gamma_{SILENT}$	0
Unit cell volume, $V$ (Å <sup>3</sup> )		117.49	121.58		$\Gamma_{RAMAN}$	$5A_g \oplus 5E_g$
Calc. density, $\rho$ (g cm <sup>-3</sup> )		5.89	5.69		$\Gamma_{INFRARED}$	$4A_u \oplus 4E_u$

With the atomic site occupation listed in table 2, we were able to predict the number and symmetry of each vibrational mode at the Brillouin zone-center ( $\mathbf{q} \simeq 0$ ) by taking the irreducible representation of the  $C_{3i}$  ( $\equiv S_6$ ) factor group [57]. The character table for this group shows that the acoustic and infrared modes belong to the  $A_u$  and  $E_u$  representations, while the  $A_g$  and  $E_g$  irreducible representations are Raman active. The distribution of the degrees of freedom for the ilmenite structure can be calculated, as shown in table 2. Cadmium

atoms are in 2c sites ( $C_3$  symmetry) and then contributing with  $A_g \oplus A_u \oplus E_g \oplus E_u$  modes. Similar site symmetry is found for the titanium atoms at 2c Wyckoff positions, while oxygen anions are at 6f sites ( $C_1$  symmetry) and providing the following representation:  $3A_g \oplus 3A_u \oplus 3E_g \oplus 3E_u$ . Therefore, ten Raman active ( $5A_g \oplus 5E_g$ ) and eight infrared ones ( $4A_u \oplus 4E_u$ ) are foreseen for the Il-type CdTiO<sub>3</sub>.

Both Raman and infrared spectra at room temperature of the Il-type CdTiO<sub>3</sub> are well documented in the literature,

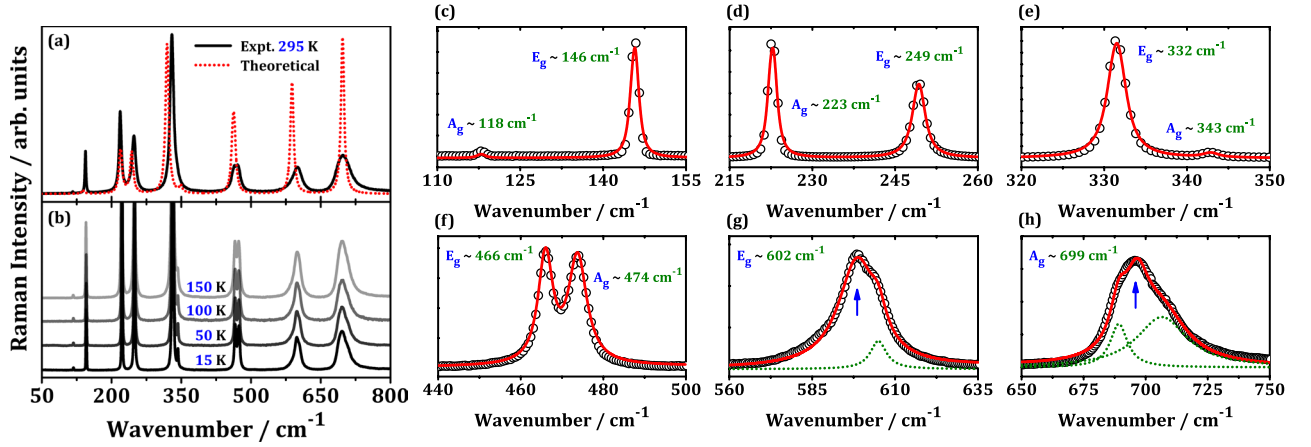


**Figure 2.** (a) Experimental and theoretical Raman spectra of Il-type CdTiO<sub>3</sub> at room condition. (b) Low temperature (15–150 K) Raman spectra of Il-type CdTiO<sub>3</sub>. (c)–(h) Decomposition process of the 15 K spectra by Lorentzian functions, where the black open circles represent the experimental data and red solid lines are the fitted spectra. In (g) and (h), the green dotted lines were included here to adjust the extra Raman bands.

**Table 3.** List of experimental (at 15 and 295 K) and calculated (DFT and SRFFM) Raman active modes ( $A_g$  and  $E_g$ ) for CdTiO<sub>3</sub> sample investigated in this paper. The parameters  $\nu_{0T}$ ,  $A$ ,  $B$ ,  $C$ , and  $D$  extracted from the Balkanski model (anharmonic constants) is also summarized for each Raman mode, except that one at 343 cm<sup>-1</sup> ( $A_g$ ). Abbreviations:  $\Omega$  = mode position; DFT = density functional theory; SRFFM = short-range force field model.

N.°	Experimental				Balkanski model parameter				
	15 K (cm <sup>-1</sup> )	295 K (cm <sup>-1</sup> )	DFT $\Omega$ (cm <sup>-1</sup> )	SRFFM $\Omega$ (cm <sup>-1</sup> )	$\nu_{0T}$ (cm <sup>-1</sup> )	$A$ (cm <sup>-1</sup> )	$B$ (cm <sup>-1</sup> )	$C$ (cm <sup>-1</sup> )	$D$ (cm <sup>-1</sup> )
<b><math>A_g</math>-like mode</b>									
1	118	116	110	132	119	—	—	-0.42	—
2	223	219	219	219	225	0.69	0.03	-1.83	—
3	343	—	348	348	—	—	—	—	—
4	474	473	460	541	476	2.91	-0.02	-1.91	-0.04
5	699	698	697	671	699	13.63	-0.49	-0.10	-0.09
<b><math>E_g</math>-like mode</b>									
1	146	144	139	122	146	0.24	—	-0.48	—
2	249	248	243	235	251	1.41	—	-0.83	-0.02
3	332	330	319	302	333	1.46	0.06	-1.29	-0.02
4	466	464	464	487	470	2.98	0.08	-3.54	-0.07
5	602	601	588	600	605	6.24	0.26	-2.72	-0.08

mainly after the work of Baran and Botto [50]. The assignment of symmetry for each optical mode in ilmenites was first introduced by Hofmeister after infrared reflectance studies on the FeTiO<sub>3</sub> natural ilmenite in its single-crystal form [58]. The author correlated the vibrational spectra of ilmenites in a set of fourteen isostructural compounds, leading to the symmetry assignment of the optical modes. These results were further confirmed through polarized Raman studies and first-principles calculation in Il-type MgTiO<sub>3</sub> [59]. In order to better characterize the optical phonons at  $\Gamma$ -point, Il-type CdTiO<sub>3</sub> was taken as a case of study in our work, being its phonon modes further predicted by density functional theory. Such predictions were also complemented by means of the SRFFM, as discussed in the following lines.

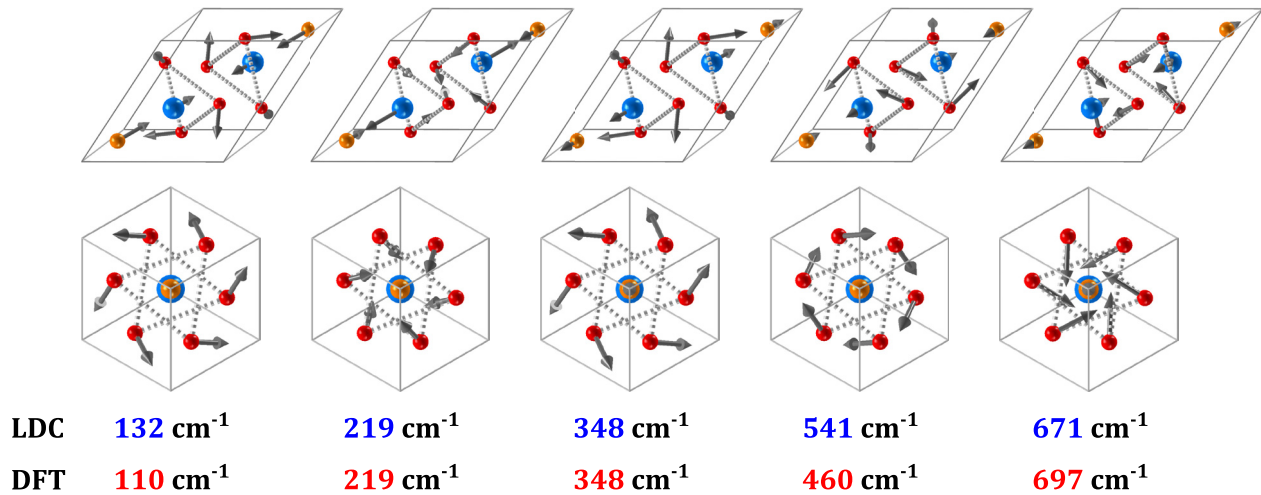
Figure 2(a) exhibits the Raman spectrum recorded at 295 K for the Il-type CdTiO<sub>3</sub> sample. From the spectral decomposition, only nine bands were detected using our experimental setup with resolution  $\leq 1$  cm<sup>-1</sup>. Such a spectrum was compared

with the calculated Raman modes derived from our theoretical model for Il-type CdTiO<sub>3</sub> by DFT methods. Both calculated and experimental Raman positions are listed in table 3 from which it can be concluded that there is a good agreement between those modes in light of the mode position. However, the predicted  $A_g$  band located at 348 cm<sup>-1</sup> is not clearly distinguished in the experimental spectrum at room temperature, probably due to thermal effects including the broadening induced by anharmonicity of the interatomic potential.

#### 4.2. Temperature-dependent Raman studies

In this way, low temperature Raman spectra were acquired for solving overlapping bands due to broadenings related to thermal effects. In figure 2(b), the 15 K spectrum for the Il-type CdTiO<sub>3</sub> can be seen. Now all the ten modes can be easily recognized. Attention should be given to the progressive occurrence of the  $A_g$  band centered at 343 cm<sup>-1</sup> when the

## $A_g$ -like modes



## $E_g$ -like modes

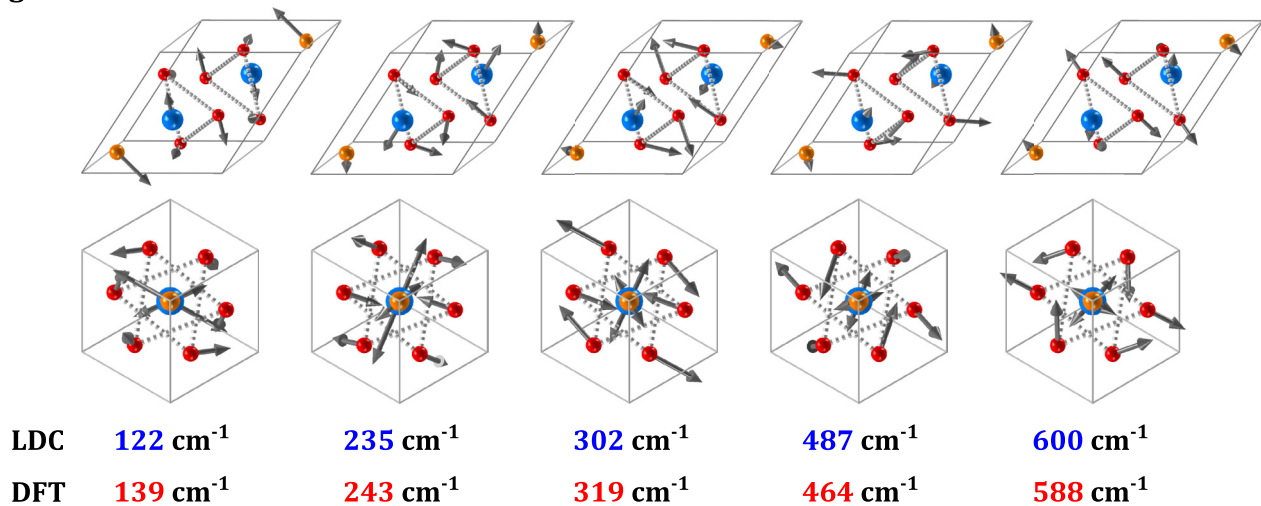


**Figure 3.** Schematic representation of the Raman active modes ( $5A_g \oplus 5E_g$ ) with calculated wavenumbers right below (LDC and DFT). The relative amplitude of the vibrations is represented by the gray arrow length. Each mode is shown in two ways: tridimensional (top-row) one and along the  $[111]_R$  projection (bottom-row). The orange, blue, and red spheres denote cadmium, titanium, and oxygen atoms, respectively.

temperature is decreased. Figures 2(c)–(h) shows the decomposition process performed in 15 K spectrum in order to determine the peak parameters for each Raman mode, as listed in table 3. It should be noticed that the high wavenumber bands in figures 2(g) and (h) showed asymmetric peak shapes as temperature decreased to 15 K. Such an asymmetry may be related to the appearing of extra modes close to  $E_g$  and  $A_g$  ones at 602 and 699 cm<sup>-1</sup>. Indeed, one and two Lorentzian functions were included during the fitting to adjust the bands in (g) and (h), respectively.

Additional Raman modes may be a signal of local symmetry lowering at low temperatures [60] or even lattice distortions at room temperature induced by occupational disorder [61, 62]. In general, the interatomic distance tends to decrease when temperature decreases, leading to local distortion that lowers the unit cell symmetry. Such a process is ruled by

the loss of some symmetry operation within the space group under study. This local symmetry breakdown can be the main key for describing the extra Raman modes in figures 2(g) and (h). A similar approach was used by Sathe *et al* to account no-predicted Raman modes at low temperature in high-quality LaAlO<sub>3</sub> single-crystal [60]. Dias *et al* also concluded that the symmetry lowering induced by local B-site disorder in Ba<sub>2</sub>YNbO<sub>6</sub> perovskites may explain the enlarged number of Raman modes detected in fired samples at lower temperatures [63]. In all the reported examples for symmetry lowering, a better understanding of the crystal structure is always required.

In light of the SRFFM, the optical phonons of the II-type CdTiO<sub>3</sub> were calculated and their atomic displacements (i.e. eigenvectors) were obtained after solving the secular equation within Wilson's *GF*-method. Table 3 compares the Raman modes predicted by DFT and SRFFM that exhibit a

good agreement. Figure 3 shows the atomic displacement patterns for all the Raman active modes in rhombohedral CdTiO<sub>3</sub>. It is noteworthy that two Cd<sup>2+</sup> ions lie at the three-fold axis ( $C_3$ ), being linked by the inversion operation. In other words, these two ions at  $2c$  sites have the next fractional coordinates:  $(x_1, x_1, x_1)$  and  $(\bar{x}_1, \bar{x}_1, \bar{x}_1)$ . Such an assumption is also valid for Ti atoms due to their position at  $2c$  sites, being described by the following coordinates:  $(x_2, x_2, x_2)$  and  $(\bar{x}_2, \bar{x}_2, \bar{x}_2)$ . In all the  $A_g$ -like modes, Cd and Ti atoms move along the  $C_3$  rotation axis, while their displacement vectors lie at orthogonal planes to this axis for  $E_g$ -like modes.

The  $A_g$  mode at  $671\text{ cm}^{-1}$  (experiment:  $698\text{ cm}^{-1}$ ) is described by the out-phase displacement of Cd and Ti atoms relative to in-plane oxygen breathing. Such a mode has major contributions coming from  $K_2$  (stretching bond Ti–O with PED  $\sim 27\%$ ) and  $F_1$  (stretching bond O–O with PED  $\sim 63\%$ ) force constants. Figure 4 summarizes the PED for each Raman active mode. On the other hand, the  $E_g$  mode at  $600\text{ cm}^{-1}$  (experiment:  $601\text{ cm}^{-1}$ ) has the out-of-plane oxygen asymmetric stretching combined with the atomic displacements of Cd and Ti atoms shifted by  $\sim 90^\circ$ . This mode has also major contributions owing to force constants  $K_2$  (PED  $\sim 26\%$ ) and  $F_1$  (PED  $\sim 50\%$ ), representing a great dependence of high wavenumber modes on the Ti atoms. Indeed, the bands above  $300\text{ cm}^{-1}$  are designated as internal modes and then representing almost pure vibrations of Ti–O<sub>3</sub> units for ilmenite system [58].

Low wavenumber bands including  $A_g \sim 132\text{ cm}^{-1}$  (experiment:  $116\text{ cm}^{-1}$ ) and  $E_g \sim 122\text{ cm}^{-1}$  (experiment:  $144\text{ cm}^{-1}$ ) represent the lattice phonons concerning the motions of Cd atoms, also known as external modes [58]. These vibrations have contributions arising from stretching bonds Cd–O ( $K_1$ ) and O–O ( $F_1$ ), and bending force for angle bond O–Cd–O ( $H_1$ ), as listed in figure 4. For this reason, any local lattice distortion can be probed by following the trend of low wavenumber Raman modes. This fact can be useful for investigations concerning the solid-solution monitoring when Cd<sup>2+</sup> ions are replaced by any divalent cation or even for structural analysis at short-range under extreme conditions, including high temperature and pressure. Hence, Raman spectra of Il-type CdTiO<sub>3</sub> were recorded in function of temperature at room pressure to better characterize its Raman modes, as discussed below.

Figures 5(a)–(c) depicts the Raman spectra collected at isothermal conditions under  $\sim 0\text{ GPa}$  in the temperature range between 15 and 1173 K. All the Raman modes at zone-center followed the anharmonic effects described by Balkanski *et al* that included the three-phonon and four-phonon processes to the broadening and shift [64]. In particular, the temperature-dependent width  $\Gamma(T)$  and position  $\Omega(T)$  (both in  $\text{cm}^{-1}$ ) can be expressed as follows, respectively,

$$\Gamma(T) = A \left[ 1 + \frac{2}{e^x - 1} \right] + B \left[ 1 + \frac{3}{e^y - 1} + \frac{3}{(e^y - 1)^2} \right], \quad (3)$$

$$\Omega(T) = \nu_{0T} + C \left[ 1 + \frac{2}{e^x - 1} \right] + D \left[ 1 + \frac{3}{e^y - 1} + \frac{3}{(e^y - 1)^2} \right], \quad (4)$$

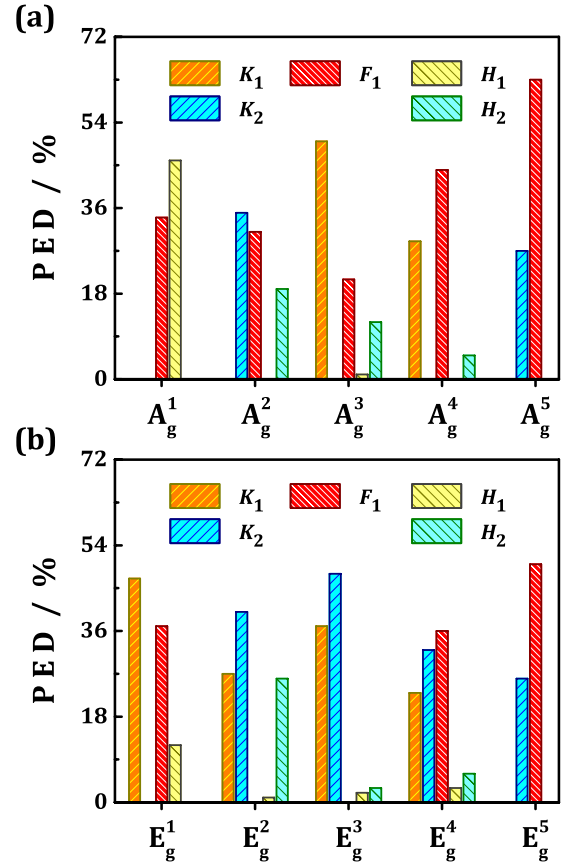


**Figure 4.** PED extracted from the classical calculations for Raman modes of Il-type CdTiO<sub>3</sub>: (a)  $A_g$ -like and (b)  $E_g$ -like symmetry species. Such a coefficient provides the percentage contribution of each force constant to an arbitrary eigenvalue.

where  $x = hc\nu_{0T}/(2k_B T)$  and  $y = hc\nu_{0T}/(3k_B T)$ ;  $\nu_{0T}$ , A, B, C and D (in  $\text{cm}^{-1}$ ) are adjustable parameters;  $h$ ,  $c$ ,  $k_B$ , and  $T$  are Planck's constant, speed of light in vacuum, Boltzmann's constant, and temperature (in K), respectively. Here, both the width and position of each Raman mode was adjusted using Lorentzian distributions and then plotted as a function of temperature.

Figures 5(d)–(i) shows the experimental and fitted data concerning temperature-dependent width and position for some Raman modes observed in (a)–(c). The thick gray lines representing the adjusted curves via equations (3) and (4) are in good agreement with the width and position parameters extracted from the experimental spectra. It can be concluded that there are no extra signals of any structural phase transition at high temperatures (until 1173 K), since the peak parameters present no deviation from the anharmonicity behavior due to higher-order terms of the vibrational Hamiltonian [64]. The values for the adjustable parameters  $\nu_{0T}$ , A, B, C and D for each Raman active mode of Il-type CdTiO<sub>3</sub> are summarized in table 3.

In general, structural phase transitions at certain temperature or even phonon interaction with spin (for magnetic materials) can be seen through deviations from the expected temperature dependence behavior in light of Balkanski model. In the latter situation, lattice vibrations modulate the



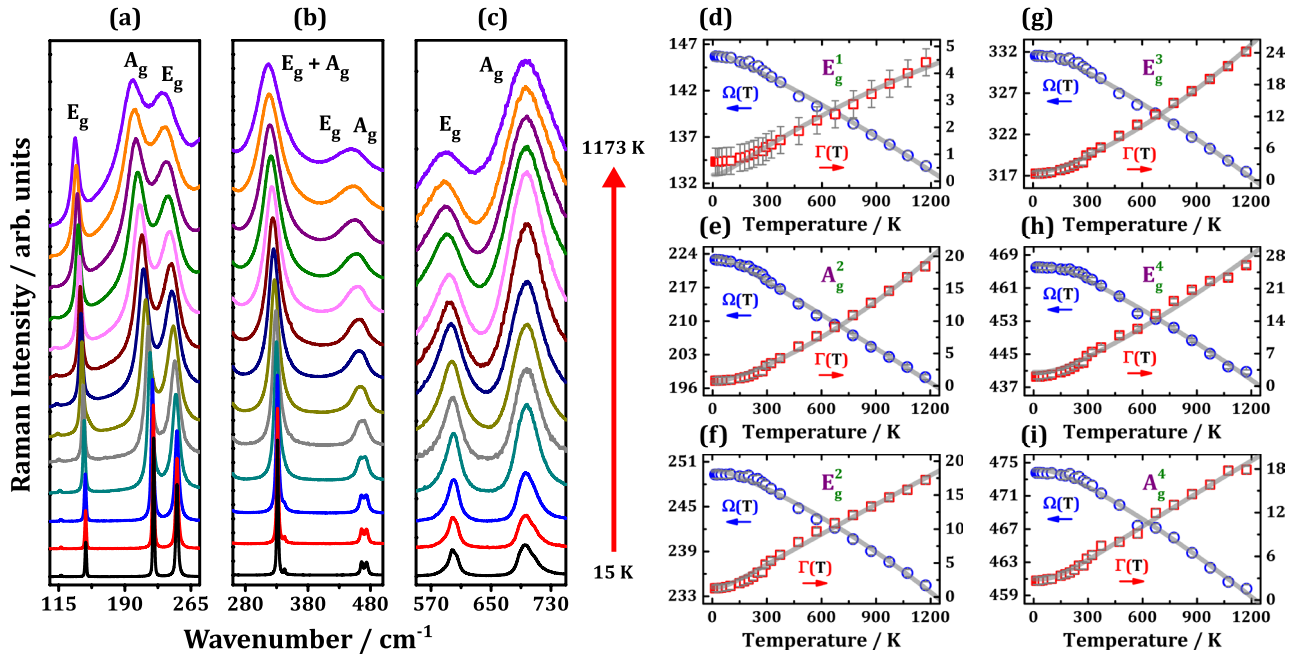


**Figure 5.** (a)–(c) Temperature dependence of the Raman active phonon spectra in the temperature range between 15 K and 1173 K. (d)–(i) Balkanski model applied to fit the temperature-dependent width  $\Gamma(T)$  and position  $\Omega(T)$  (both in  $\text{cm}^{-1}$ ) of some Raman bands in (a)–(c). Red open squares and blue open circles represent the width and position, respectively, and the thick gray lines denote the adjusted curves.

magnetic exchange interaction in insulating magnets and the departure from the anharmonic behavior will be proportional to the spin-spin correlation function  $\langle S_i \cdot S_j \rangle$  between nearest magnetic ions [65, 66]. In the former case, new optical modes may arise from a change in space group, bringing new selection rules for Raman and infrared activity [67–70]. This trend is usually detected when the temperature is decreased and then revealing a lower symmetry crystal structure. In figure 5, instead, none of these features is detected in our temperature-dependent Raman studies in II-type CdTiO<sub>3</sub>, although the peak asymmetry as a result of possible new bands was clearly noticed in high wavenumber intervals of figures 2(g) and (h).

In order to explain the peak asymmetry in low temperature Raman spectra, we propose a structural model considering the local loss of the inversion symmetry within rhombohedral  $R\bar{3}$  space group. Firstly, we assume that low temperature condition induces a decrease in the Ti–O bond length and then elevating the degree of distortion of the ilmenite structure. Therefore, the constraint over the Ti atoms coordinates due to inversion symmetry is no longer valid and, consequently, splitting the  $2c$  Wyckoff sites into two parts. The remaining symmetry operations will describe the rhombohedral  $R\bar{3}$  space group ( $C_3^4$  or #146), and the new site symmetries are listed in table 4. Now, each atom has two non-equivalent positions and, particularly, two Cd atoms are in two  $1a$  site and providing the following reducible representation  $2A \oplus 2E$ . The titanium atoms have the similar site symmetry at two  $1a$  Wyckoff sites, while six oxygen anions are at two  $3b$  sites and giving  $\Gamma_O = 6A \oplus 6E$ . Notice that in  $R\bar{3}$  space group,  $A$  and  $E$  irreducible representations are both Raman and infrared active due the loss of the mutual exclusion rule of states. The phonon activity, for Raman scattering and infrared absorption,

**Table 4.** Nuclear site group analysis for the II-type CdTiO<sub>3</sub> with rhombohedral unit cell belonging to the  $R\bar{3}$  ( $C_3^4$  or #146) space group. Such a crystal structure is directly derived from the  $R\bar{3}$  space group when inversion symmetry is missing.  $A$  and  $E$  irreducible representations are both Raman and infrared active.

Atom	Wyckoff site	symmetry	Irreducible representation
Cd <sub>1</sub>	$1a$	3. ( $C_3$ )	$A \oplus E$
Cd <sub>2</sub>	$1a$	3. ( $C_3$ )	$A \oplus E$
Ti <sub>1</sub>	$1a$	3. ( $C_3$ )	$A \oplus E$
Ti <sub>2</sub>	$1a$	3. ( $C_3$ )	$A \oplus E$
O <sub>1</sub>	$3b$	1 ( $C_1$ )	$3A \oplus 3E$
O <sub>2</sub>	$3b$	1 ( $C_1$ )	$3A \oplus 3E$
$\Gamma_{\text{TOTAL}} = 10A \oplus 10E$			$\Gamma_{\text{RAMAN}} = 9A \oplus 9E$
$\Gamma_{\text{ACOUSTIC}} = A \oplus E$			$\Gamma_{\text{INFRARED}} = 9A \oplus 9E$

predicted by factor group analysis is listed in table 4. Hence, it is expected 18 Raman modes ( $9A \oplus 9E$ ) at  $\Gamma$ -point for  $C_3$  point group. In summary, the increase in the number of predicted Raman modes seems to agree with the extra bands in figures 2(g) and (h).

#### 4.3. Pressure-dependent Raman studies

We will extend our theoretical analysis based on group-theory to confirm the earlier model in describing the enlarged number of Raman modes at low temperature. An alternative method for reducing the atomic bond is to put the material under high hydrostatic pressure conditions [71, 72]. In this way, Raman spectra for the II-type CdTiO<sub>3</sub> were recorded under pressure at room temperature. Figures 6(a), (b) and 7(a), (b) illustrate the pressure-dependent Raman spectra from  $\sim 0$  up to 18.5 GPa. It is also exhibited the pressure-dependent Raman spectra

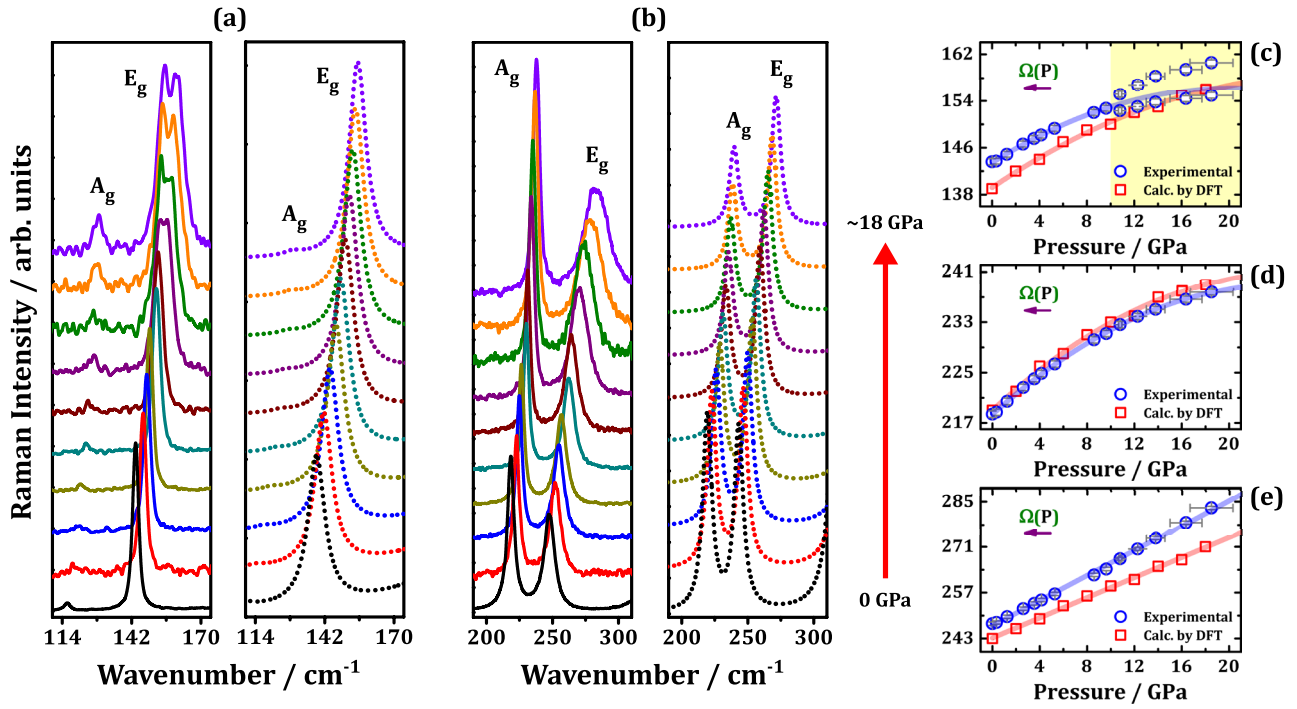


**Figure 6.** (a) and (b) Experimental (solid lines) and calculated (dotted lines) Raman spectra, in the low wavenumber range 100–300 cm<sup>-1</sup>, at different pressures between ~0 and 18.5 GPa. Parts (c)–(e) depict a comparison between experimental (blue open squares) and calculated (red open circles) pressure-dependent mode position  $\Omega(P)$  for some Raman bands in (a) and (b). Attention should be given to the splitting of E<sub>g</sub> mode at 144 cm<sup>-1</sup> in (c), which was attributed to a local symmetry lowering due to a loss of inversion operation.

calculated from DFT methods. As a whole, the mode position undergoes a blueshift as the hydrostatic pressure was increased. However, most of the Raman modes maintain their profile, except that one at 144 cm<sup>-1</sup> (E<sub>g</sub>) that shows a splitting for pressures higher than ~10 GPa, seen in figure 6(c). Such a behavior was not seen in our theoretical Raman spectra under hydrostatic pressure. Based on these data, the pressure dependences of the position  $\Omega(P)$  for all the experimental and theoretical Raman modes were determined and further adjusted by the following equation:

$$\Omega(P) = \nu_{0P} + \left(\frac{\partial\Omega}{\partial P}\right)_T P - \frac{1}{2} \left(\frac{\partial^2\Omega}{\partial P^2}\right)_T P^2, \quad (5)$$

such that  $\nu_{0P}$ ,  $(\partial\Omega/\partial P)_T$  and  $(\partial^2\Omega/\partial P^2)_T$  denotes the mode position at room pressure (~0 GPa), its linear and quadratic pressure coefficients, respectively. Such parameters were calculated from the fittings of the experimental and theoretical data, as shown in figures 6(c)–(e), summarized in table 5 for each Raman active mode. The quadratic dependence on hydrostatic pressure was only found for the low wavenumber modes in II-type CdTiO<sub>3</sub>. Similar quadratic behavior was also reported for other oxides [73, 74]. Both experimental and theoretical mode Grüneisen parameters ( $\gamma$ ) for the Raman bands are also quoted in table 5. These parameters can be derived from the next expression:

$$\gamma = \frac{B_0}{\nu_{0P}} \left(\frac{\partial\Omega}{\partial P}\right)_T. \quad (6)$$

It can be concluded that there is a reasonable agreement between the experimental and theoretical mean  $\gamma$  parameter, since  $\langle\gamma_{\text{exp}}\rangle = 1.33$  and  $\langle\gamma_{\text{DFT}}\rangle = 1.28$ .

In our DFT calculations, the optical phonons were simulated under hydrostatic condition starting from 0 to 18 GPa, with an increment of 2 GPa. One can note that there is a good agreement between experimental and calculated data, mainly concerning the blueshift of all the Raman modes as pressure increases. Note that our structural model was capable of describing a second splitting of the E<sub>g</sub> and A<sub>g</sub> modes at 464 and 473 cm<sup>-1</sup>, respectively. However, none of these features were foreseen for the E<sub>g</sub> mode at 144 cm<sup>-1</sup>. It is important to highlight that all the symmetry operations within  $R\bar{3}$  space group were conserved during high-pressure simulations and then ten Raman modes ( $5A_g \oplus 5E_g$ ) were always kept. A second point is that high-pressure experiments were performed by taking 16:4:1 methanol–ethanol–water mixture as a PTM. Such a medium has a glass transition close to 10 GPa and hence the ideal hydrostatic condition begins to be lost as a consequence of the fluid solidification [75, 76].

In a nonhydrostatic condition, the stress state should be described by both normal  $\sigma_{ii}$  and shear  $\sigma_{ij}$  ( $i \neq j$ ) components to define the deviatoric stress tensor [77]. In addition, all the components of this tensor will represent the stress state of the medium and hence defining a spatial inhomogeneity. For high-pressure structural studies, such a condition is not desired, since anomalies in a given physical property at the fluid vitrification pressure can be misinterpreted [78, 79]. In a particular situation in which  $\sigma_{ij} = 0$  (without shear stress) and the external force is almost unidirectional, the normal components are  $\sigma_x = \sigma_y \neq \sigma_z$  that defines the uniaxial compression condition. Both nonhydrostatic and uniaxial situations should occur after the PTM glass transition. The detection of the loss of hydrostaticity can be performed by the ruby fluorescence

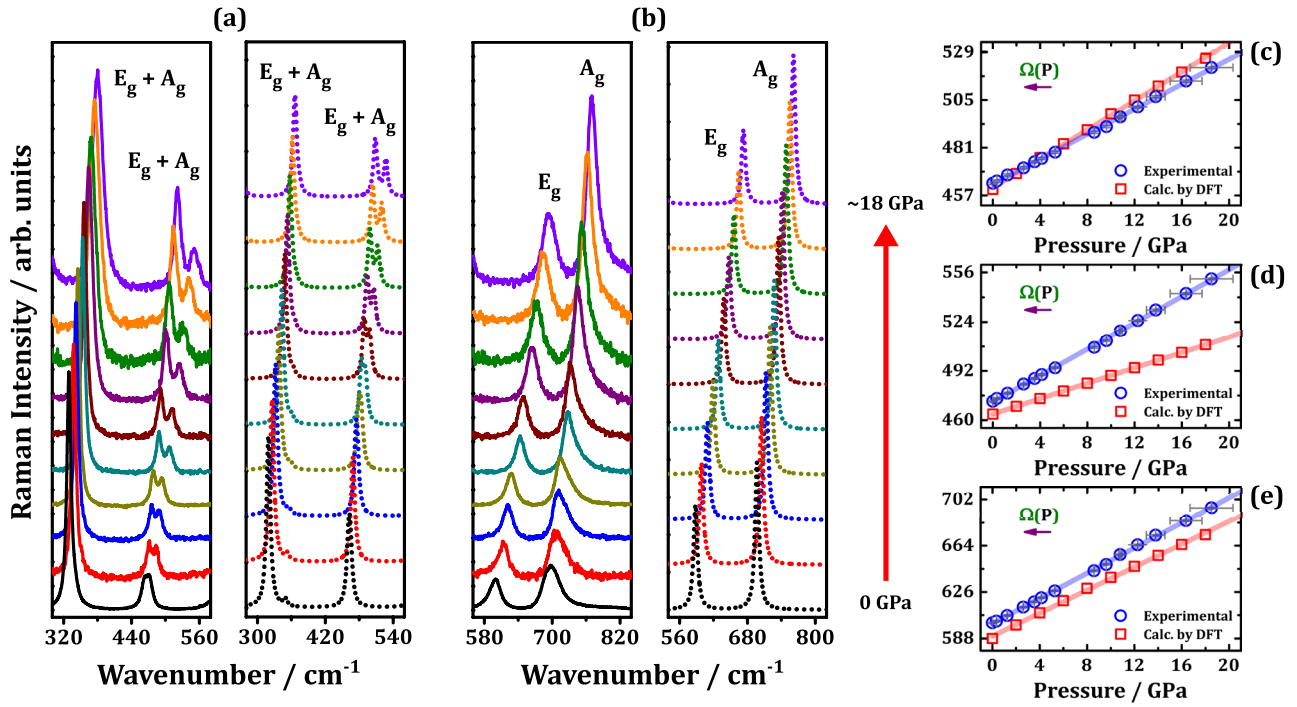


**Figure 7.** (a) and (b) Experimental (solid lines) and calculated (dotted lines) Raman spectra, in the high wavenumber range 300–800  $\text{cm}^{-1}$ , at different pressures between  $\sim 0$  and 18.5 GPa. Parts (c)–(e) depict a comparison between experimental (blue open squares) and calculated (red open circles) pressure-dependent mode position  $\Omega(P)$  for some Raman bands in (a) and (b).

**Table 5.** Experimental and theoretical data on the pressure dependence of each Raman mode. The parameters  $\nu_{0P}$ ,  $(\frac{\partial\Omega}{\partial P})_T$ , and  $(\frac{\partial^2\Omega}{\partial P^2})_T$  represent the mode position at room pressure ( $\sim 0$  GPa), its linear and quadratic pressure coefficients, respectively. It also summarized the calculated mode Grüneisen parameter  $\gamma$  using theoretical  $B_0$  ( $=163$  GPa), in which exp = extracted from experimental data and DFT = calculated via density functional theory.

N.°	Experimental data				Theoretical data			
	$\nu_{0P}$ ( $\text{cm}^{-1}$ )	$(\frac{\partial\Omega}{\partial P})_T$ ( $\text{cm}^{-1} \text{GPa}^{-1}$ )	$\frac{1}{2}(\frac{\partial^2\Omega}{\partial P^2})_T$ ( $\text{cm}^{-1} \text{GPa}^{-2}$ )	$\gamma_{\text{exp}}$	$\nu_{0P}$ ( $\text{cm}^{-1}$ )	$(\frac{\partial\Omega}{\partial P})_T$ ( $\text{cm}^{-1} \text{GPa}^{-1}$ )	$\frac{1}{2}(\frac{\partial^2\Omega}{\partial P^2})_T$ ( $\text{cm}^{-1} \text{GPa}^{-2}$ )	$\gamma_{\text{DFT}}$
<b>A<sub>g</sub>-like mode</b>								
1	115	1.23	0.03	1.77	110	1.78	0.04	2.64
2	218	1.69	0.03	1.26	219	1.74	0.03	1.30
3	—	—	—	—	349	1.34	—	0.63
4	472	4.29	—	1.48	464	2.50	—	0.88
5	698	3.93	—	0.92	698	3.56	—	0.83
<b>E<sub>g</sub>-like mode</b>								
1	143	1.27	0.03	1.44	139	1.37	0.03	1.60
2	247	1.92	—	1.26	243	1.53	—	1.03
3	330	2.75	—	1.36	321	2.58	—	1.31
4	463	3.14	—	1.11	461	3.65	—	1.29
5	600	5.17	—	1.40	590	4.71	—	1.30

technique in which  $\delta R = R_1 - R_2$  splitting detects uniaxial stress, while  $R_1$  and  $R_2$  widths are sensitive to the stress inhomogeneity [80, 81]. Nevertheless,  $R_1$  line may maintain its pressure scale feature [82]. Figure S2(a) depicts the ruby luminescence spectra in a 16:4:1 methanol–ethanol–water mixture, while (b) shows the pressure dependence of  $R$ -lines width and  $\delta R$  splitting, respectively. It can be seen that  $\delta R$  splitting starts to increase at the vitrification pressure of  $\sim 10$  GPa, besides the broadening of the  $R$ -lines. Such facts enable us to conclude that a complex stress state with inhomogeneity occurred at pressures higher than 10 GPa.

In practice, the spatial inhomogeneity leads to a lattice distortion in the crystal structure that can be seen through the splitting of  $d$ -spacings, as reported by Singh *et al* [83]. Keeping in mind the earlier facts, we may conclude that the stress state above  $\sim 10$  GPa induced a distortion in the rhombohedral lattice of II-type  $\text{CdTiO}_3$ . Particularly, the splitting process of  $\mathbf{E}_g$  mode at  $144 \text{ cm}^{-1}$  in figure 6(c) can be also understood as a local symmetry lowering due to a loss of inversion operation. Our results show that the vibrational displacements involving the Cd atoms are sensitive to lattice distortions and hence to symmetry lowering. The structural model described in table 4

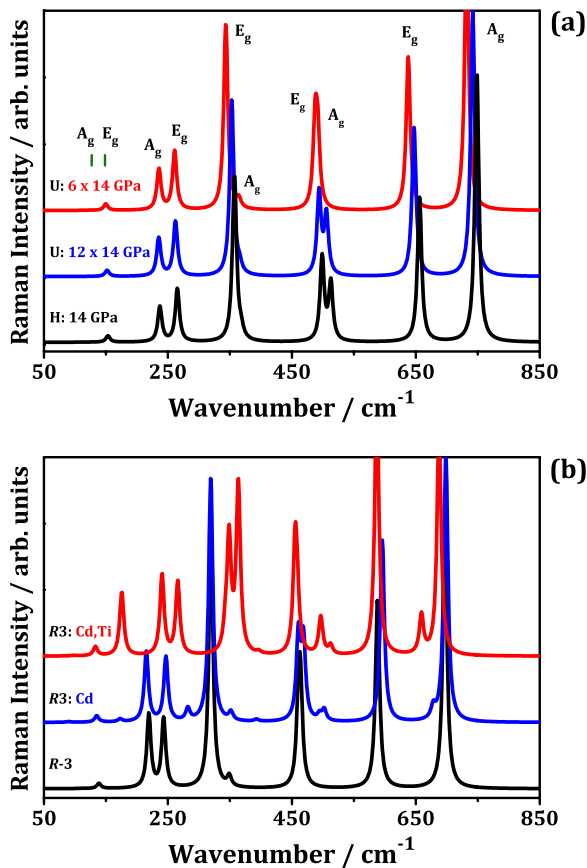


**Figure 8.** Two theoretical scenarios were evaluated in order to explain the extra Raman in both low temperature (under vacuum condition) and high-pressure (at room temperature) spectra: (a) uniaxial compression and (b) broken inversion symmetry as quoted in the structural model of table 4. Additional Raman modes are only seen in a less symmetric crystal structure.

is useful to elucidate that the inversion symmetry breaking takes place during the stress state at the vitrification pressure. A piece of evidence for this fact comes from figure S3 that exhibits the calculated pressure dependence of relative fractional coordinates of Cd and Ti atoms. It can be observed that the Cd atom coordinates are more affected than those for Ti atoms at high hydrostatic pressure condition.

In this sense, we applied our optimized theoretical model for II-type CdTiO<sub>3</sub> in order to evaluate two scenarios. In figure 8(a), calculated Raman spectra under uniaxial compression are shown, in which all the predicted modes ( $5A_g \oplus 5E_g$ ) are assigned. One may conclude that the uniaxial condition is not enough to explain the extra Raman mode detected above  $\sim 10$  GPa. In figure 8(b), however, Raman spectra were calculated starting from a less symmetric rhombohedral *R3* unit cell. Two situations were simulated for probing the effect of off-center displacement of Cd and Ti atoms, for which the structural model listed in table 4 was taken into account. In the first case, only one Cd atom is off-centered. In the second case, instead, both Cd and Ti atoms present off-center displacement. Now, extra Raman modes are seen for the simulated situations and the complete set of 18 Raman modes ( $9A \oplus 9E$ ) is summarized in table S2, elucidating that the proposed model

for the local loss of inversion symmetry has physical bases to explain the enlarged number of Raman modes in II-type CdTiO<sub>3</sub> at low temperature (vacuum condition) and under high-pressure (ambient temperature).

## 5. Summary and conclusion

In summary, we combined experimental and theoretical methods in order to investigate the lattice dynamics of CdTiO<sub>3</sub> in its rhombohedral  $C_{3i}^2$  ( $R\bar{3}$ ) ilmenite phase. The samples were successfully synthesized using the solid state method and its crystal structure was refined by Rietveld method. Based on this data, a theoretical model was built in *CRYSTAL17* program to provide Raman and infrared data through second derivatives of the total energy. We also employed a classical methodology based on the ionic short-range interaction to describe the optical modes in II-type CdTiO<sub>3</sub>, in which three stretching and two bending force constants were considered to parameterize the nearest neighbor interactions. Both experimental and calculated optical phonons are in reasonable agreement. Important physical parameters were also provided, including the bulk modulus, anharmonic constants, and Grüneisen parameters. Extra Raman modes were observed in two situations, at low temperature (under vacuum condition) and under high-pressure (at room temperature), which cannot be accounted for the factor group analysis of the  $C_{3i}$  point group. As a consequence of bond distance decrease at low temperature, we proposed a structural model considering a broken inversion symmetry which reduces the  $C_{3i}$  point group to the  $C_3$  one. In  $C_3^4$  (*R3*) space group, the 18 predicted Raman modes ( $9A \oplus 9E$ ) are in agreement with the extra modes observed for II-type CdTiO<sub>3</sub>. The local loss of inversion symmetry also occurred in a nonhydrostatic condition, above the glass transition of the PTM. We argued that the stress state induces a lattice distortion capable of lowering the crystal symmetry of II-type CdTiO<sub>3</sub>. The above results, which can be extended to other ATiO<sub>3</sub>-ilmenite compounds, show that the combination of theoretical and experimental approaches is fundamental to probe local structure in materials.

## Acknowledgments

The authors are grateful to the Brazilian funding agencies: CAPES (Proc. Numbers 787027/2013 and 8881.068492/2014-01), CNPq (Proc. Number 150936/2017-6), and FAPESP (Proc. Numbers 2013/07793-6, 2013/07296-2, and 2016/07476-9) for the financial support.

## ORCID iDs

J E Rodrigues <https://orcid.org/0000-0002-9220-5809>  
 M M Ferrer <https://orcid.org/0000-0002-0484-0192>  
 T R Cunha <https://orcid.org/0000-0003-1114-5208>  
 P S Pizani <https://orcid.org/0000-0002-5914-1671>

## References

- [1] Xiao Y, Zhang C, Zhang X, Cai G, Zheng Y, Zheng Y, Zhong F and Jiang L 2017 A novel highly sensitive NO<sub>2</sub> sensor based on perovskite Na<sub>0.5+x</sub>Bi<sub>0.5</sub>TiO<sub>3-δ</sub> electrolyte *Sci. Rep.* **7** 4997
- [2] Wang H and Kim D H 2017 Perovskite-based photodetectors: materials and devices *Chem. Soc. Rev.* **46** 5204–36
- [3] Grinberg I et al 2013 Perovskite oxides for visible-light-absorbing ferroelectric and photovoltaic materials *Nature* **503** 509–12
- [4] Webber K G, Vögler M, Khansur N H, Kaeswurm B, Daniels J E and Schader F H 2017 Review of the mechanical and fracture behavior of perovskite lead-free ferroelectrics for actuator applications *Smart Mater. Struct.* **26** 063001
- [5] Ng C H, Lim H N, Hayase S, Harrison I, Pandikumar A and Huang N M 2015 Potential active materials for photo-supercapacitor: a review *J. Power Sources* **296** 169–85
- [6] Sebastian M T, Uvic R and Jantunen H 2015 Low-loss dielectric ceramic materials and their properties *Int. Mater. Rev.* **60** 392–412
- [7] Xue K-H, Fonseca L R C and Miao X-S 2017 Ferroelectric fatigue in layered perovskites from self-energy corrected density functional theory *RSC Adv.* **7** 21856–68
- [8] Hikami S and Matsuda Y 1987 High T<sub>c</sub> superconductors of the perovskite structure oxides *Japan. J. Appl. Phys.* **26** 1027
- [9] Liu Y, Crespillo M L, Huang Q, Wang T J, Liu P and Wang X L 2017 Lattice damage assessment and optical waveguide properties in LaAlO<sub>3</sub> single crystal irradiated with swift Si ions *J. Phys. D: Appl. Phys.* **50** 055303
- [10] Bhalla A S, Guo R and Roy R 2000 The perovskite structure—a review of its role in ceramic science and technology *Mater. Res. Innov.* **4** 3–26
- [11] Yu Z-L, Ma Q-R, Zhao Y-Q, Liu B and Cai M-Q 2018 Surface termination—a key factor to influence electronic and optical properties of CsSnI<sub>3</sub> *J. Phys. Chem. C* **122** 9275–82
- [12] Zhao Y Q, Liu B, Yu Z L, Ma J M, Wan Q, He P B and Cai M Q 2017 Strong ferroelectric polarization of CH<sub>3</sub>NH<sub>3</sub>GeI<sub>3</sub> with high-absorption and mobility transport anisotropy: theoretical study *J. Mater. Chem. C* **5** 5356–64
- [13] Zhao Y-Q, Ma Q-R, Liu B, Yu Z-L, Yang J and Cai M-Q 2018 Layer-dependent transport and optoelectronic property in two-dimensional perovskite: (PEA)<sub>2</sub>PbI<sub>4</sub> *Nanoscale* **10** 8677–88
- [14] Liu B, Zhao Y-Q, Yu Z-L, Wang L-Z and Cai M-Q 2018 Tuning the Schottky rectification in graphene-hexagonal boron nitride-molybdenum disulfide heterostructure *J. Colloid Interface Sci.* **513** 677–83
- [15] Galasso F S, Smoluchowski R and Kurti N 1969 *Structure, Properties and Preparation of Perovskite-Type Compounds* (Amsterdam: Elsevier)
- [16] Slater J 1950 The Lorentz correction in barium titanate *Phys. Rev.* **78** 748–61
- [17] Shirane G, Suzuki K and Takeda A 1952 Phase transitions in solid solutions of PbZrO<sub>3</sub> and PbTiO<sub>3</sub> (II) x-ray study *J. Phys. Soc. Japan* **7** 12–8
- [18] Glazer A M 1975 Simple ways of determining perovskite structures *Acta Crystallogr. A* **31** 756–62
- [19] Howard C J 2005 Structures and phase transitions in perovskites—a group-theoretical approach *Acta Crystallogr. A* **61** 93–111
- [20] Woodward P M 1997 Octahedral tilting in perovskites. I. Geometrical considerations *Acta Crystallogr. B* **53** 32–43
- [21] Baraton M I, Busca G, Prieto M C, Ricchiardi G and Escribano V S 1994 On the vibrational spectra and structure of FeCrO<sub>3</sub> and of the ilmenite-type compounds CoTiO<sub>3</sub> and NiTiO<sub>3</sub> *J. Solid State Chem.* **112** 9–14
- [22] Liu X C, Hong R and Tian C 2009 Tolerance factor and the stability discussion of ABO<sub>3</sub>-type ilmenite *J. Mater. Sci., Mater. Electron.* **20** 323–7
- [23] Pataquiva-Mateus A Y, Zea H R and Ramirez J H 2017 Degradation of Orange II by Fenton reaction using ilmenite as catalyst *Environ. Sci. Pollut. Res.* **24** 6187–94
- [24] Zhang T, Shen Y and Zhang R 1995 Ilmenite structure-type β-CdSnO<sub>3</sub> used as an ethanol sensing material *Mater. Lett.* **23** 69–71
- [25] Yu L, Liu J, Xu X, Zhang L, Hu R, Liu J, Ouyang L, Yang L and Zhu M 2017 Ilmenite nanotubes for high stability and high rate sodium-ion battery anodes *ACS Nano* **11** 5120–9
- [26] Schweinler H C 1952 Ferroelectricity in the ilmenite structure *Phys. Rev.* **87** 5–11
- [27] Kennedy B J, Zhou Q and Avdeev M 2011 The ferroelectric phase of CdTiO<sub>3</sub>: a powder neutron diffraction study *J. Solid State Chem.* **184** 2987–93
- [28] Torgashev V I, Yuzyuk Y I, Shirokov V B, Lemanov V V and Spektor I E 2005 Raman spectra of cadmium titanate *Phys. Solid State* **47** 337–46
- [29] Kennedy B J, Zhou Q, Zhao S, Jia F, Ren W and Knight K S 2017 Low-temperature structure and the ferroelectric phase transitions in the CdTiO<sub>3</sub> perovskite *Phys. Rev. B* **96** 214105
- [30] Liebermann R C 1976 Elasticity of the ilmenite—perovskite phase transformation in CdTiO<sub>3</sub> *Earth Planet. Sci. Lett.* **29** 326–32
- [31] Kabirov Y V, Kul B S and Kupriyanov M F 2001 Structural phase transitions in CdTiO<sub>3</sub> *Phys. Solid State* **43** 1968
- [32] Martin G and Hegenbarth E 1973 The influence of hydrostatic pressure on the ferroelectric phase transition of CdTiO<sub>3</sub> ceramics *Phys. Status Solidi* **18** K151–2
- [33] Moriwake H, Kuwabara A, Fisher C A J, Taniguchi H, Itoh M and Tanaka I 2011 First-principles calculations of lattice dynamics in CdTiO<sub>3</sub> and CaTiO<sub>3</sub>: phase stability and ferroelectricity *Phys. Rev. B* **84** 1–8
- [34] Liebertz J and Rooymans C J M 1965 Die ilmenit/perowskitphasenumwandlung von CdTiO<sub>3</sub> unter hohem druck Z. *Phys. Chem.* **44** 242–9
- [35] Bleicher L, Sasaki J M and Paiva Santos C O 2000 Development of a graphical interface for the Rietveld refinement program DBWS *J. Appl. Crystallogr.* **33** 1189
- [36] Rietveld H M 1967 Line profiles of neutron powder-diffraction peaks for structure refinement *Acta Crystallogr.* **22** 151–2
- [37] Long D A 2002 *The Raman Effect: A Unified Treatment of the Theory of Raman Scattering by Molecules* (Chichester: Wiley)
- [38] Mao H K, Xu J and Bell P M 1986 Calibration of the ruby pressure gauge to 800 Kbar under quasi-hydrostatic conditions *J. Geophys. Res.* **91** 4673
- [39] Chijioke A D, Nellis W J, Soldatov A and Silvera I F 2005 The ruby pressure standard to 150 GPa *J. Appl. Phys.* **98** 114905
- [40] Becke A D 1993 Density-functional thermochemistry. III. The role of exact exchange *J. Chem. Phys.* **98** 5648–52
- [41] Lee C, Yang W and Parr R G 1988 Development of the Colle–Salvetti correlation-energy formula into a functional of the electron density *Phys. Rev. B* **37** 785–9
- [42] Dovesi R et al 2018 Quantum-mechanical condensed matter simulations with CRYSTAL *Wiley Interdiscip. Rev. Comput. Mol. Sci.* **8** e1360
- [43] Laun J, Vilela Oliveira D and Bredow T 2018 Consistent gaussian basis sets of double- and triple-zeta valence with polarization quality of the fifth period for solid-state calculations *J. Comput. Chem.* **39** 1285–90
- [44] Sophia G, Baranek P, Sarrazin C, Rérat M and Dovesi R 2013 First-principles study of the mechanisms of the pressure-induced dielectric anomalies in ferroelectric perovskites *Phase Transit.* **86** 1069–84

- [45] Maschio L, Kirtman B, Orlando R and R  r  t M 2012 *Ab initio* analytical infrared intensities for periodic systems through a coupled perturbed Hartree–Fock/Kohn–Sham method *J. Chem. Phys.* **137** 204113
- [46] Maschio L, Kirtman B, R  r  t M, Orlando R and Dovesi R 2013 *Ab initio* analytical Raman intensities for periodic systems through a coupled perturbed Hartree–Fock/Kohn–Sham method in an atomic orbital basis. II. Validation and comparison with experiments *J. Chem. Phys.* **139** 164102
- [47] Kothari L S, Ghatak A K and Bala S 1971 Transverse vibrations of linear and layer lattices *Am. J. Phys.* **39** 166–72
- [48] Dowty E 1987 Fully automated microcomputer calculation of vibrational spectra *Phys. Chem. Miner.* **14** 67–79
- [49] Wilson E B, Decius J C and Cross P C 1955 *Molecular Vibrations: The Theory of Infrared and Raman Vibrational Spectra* (New York: Dover)
- [50] Baran E J and Botto I L 1979 Die Raman-spektren von  $\text{ZnTiO}_3$  und  $\text{CdTiO}_3$  *Z. Anorg. Allg. Chem.* **448** 188–92
- [51] Catchen G L, Wukitch S J, Spaar D M and Blaszkiewicz M 1990 Temperature dependence of the nuclear quadrupole interactions at Ti sites in ferroelectric  $\text{PbTiO}_3$  and in ilmenite and perovskite  $\text{CdTiO}_3$ : evidence for order-disorder phenomena *Phys. Rev. B* **42** 1885–94
- [52] Birch F 1947 Finite elastic strain of cubic crystals *Phys. Rev.* **71** 809–24
- [53] Wilson N C, Muscat J, Mkhonto D, Ngoepe P E and Harrison N M 2005 Structure and properties of ilmenite from first principles *Phys. Rev. B* **71** 75202
- [54] Wu X, Qin S and Dubrovinsky L 2011 Investigation into high-pressure behavior of  $\text{MnTiO}_3$ : x-ray diffraction and Raman spectroscopy with diamond anvil cells *Geosci. Frontiers* **2** 107–14
- [55] Inaguma Y, Aimi A, Shirako Y, Sakurai D, Mori D, Kojitani H, Akaogi M and Nakayama M 2014 High-pressure synthesis, crystal structure, and phase stability relations of a  $\text{LiNbO}_3$ -type polar titanate  $\text{ZnTiO}_3$  and its reinforced polarity by the second-order Jahn–Teller effect *J. Am. Chem. Soc.* **136** 2748–56
- [56] Xin C, Wang Y, Sui Y, Wang Y, Wang X, Zhao K, Liu Z, Li B and Liu X 2014 Electronic, magnetic and multiferroic properties of magnetoelectric  $\text{NiTiO}_3$  *J. Alloys Compd.* **613** 401–6
- [57] Rousseau D L, Bauman R P and Porto S P S 1981 Normal mode determination in crystals *J. Raman Spectrosc.* **10** 253–90
- [58] Hofmeister A 1993 IR reflectance spectra of natural ilmenite: comparison with isostructural compounds and calculation of thermodynamic properties *Eur. J. Miner.* **5** 281–95
- [59] Wang C H, Jing X P, Feng W and Lu J 2008 Assignment of Raman-active vibrational modes of  $\text{MgTiO}_3$  *J. Appl. Phys.* **104** 034112
- [60] Sathe V G and Dubey A 2007 Broken symmetry in  $\text{LaAlO}_3$  single crystal probed by resonant Raman spectroscopy *J. Phys.: Condens. Matter* **19** 382201
- [61] Ayala A, Paschoal C, Guedes I, Paraguassu W, Freire P, Mendes Filho J, Moreira R and Gesland J-Y 2002 Disorder-induced symmetry lowering in the  $\text{CsInMgF}_6$  pyrochlore crystal *Phys. Rev. B* **66** 214105
- [62] Marcondes S P, Rodrigues J E F S, Andreetta M R B and Hernandez A C 2014 Resonance Raman spectroscopy of  $\text{NdAlO}_3$  single-crystal fibers grown by the laser-heated pedestal growth technique *Vib. Spectrosc.* **73** 144–9
- [63] Dias A, S  r  g G and Moreira R L 2008 Disorder-induced symmetry lowering in  $\text{Ba}(\text{Y}_{1/2}\text{Nb}_{1/2})\text{O}_3$  ceramics probed by Raman spectroscopy *J. Raman Spectrosc.* **39** 1805–10
- [64] Balkanski M, Wallis R and Haro E 1983 Anharmonic effects in light scattering due to optical phonons in silicon *Phys. Rev. B* **28** 1928–34
- [65] Granado E, Garc  a A, Sanjurjo J A, Rettori C, Torriani I, Prado F, S  nchez R D, Caneiro A and Oseroff S B 1999 Magnetic ordering effects in the Raman spectra of  $\text{La}_{1-x}\text{Mn}_{1-x}\text{O}_3$  *Phys. Rev. B* **60** 11879–82
- [66] Granado E *et al* 1998 Phonon Raman scattering in  $R_{1-x}A_x\text{MnO}_{3+\delta}$  ( $R = \text{La, Pr}$ ;  $A = \text{Ca, Sr}$ ) *Phys. Rev. B* **58** 11435–40
- [67] Islam M A, Rondinelli J M and Spanier J E 2013 Normal mode determination of perovskite crystal structures with octahedral rotations: theory and applications *J. Phys.: Condens. Matter* **25** 175902
- [68] Mart  n-Carr  n L, De Andr  s A, Mart  nez-Lope M J, Casais M T and Alonso J A 2002 Raman phonons as a probe of disorder, fluctuations, and local structure in doped and undoped orthorhombic and rhombohedral manganites *Phys. Rev. B* **66** 174303
- [69] Shigenari T 1973 On the Raman activity of soft modes in the lower symmetry phase of crystals *Phys. Lett. A* **46** 243–4
- [70] Yuzyuk Y I 2012 Raman scattering spectra of ceramics, films, and superlattices of ferroelectric perovskites: a review *Phys. Solid State* **54** 1026–59
- [71] Maul J, Erba A, Santos I M G, Sambrano J R and Dovesi R 2015 In silico infrared and Raman spectroscopy under pressure: the case of  $\text{CaSnO}_3$  perovskite *J. Chem. Phys.* **142** 14505
- [72] Ovsyannikov S V, Bykova E, Bykov M, Wenz M D, Pakhomova A S, Glazyrin K, Liermann H-P and Dubrovinsky L 2015 Structural and vibrational properties of single crystals of scandia,  $\text{Sc}_2\text{O}_3$  under high pressure *J. Appl. Phys.* **118** 165901
- [73] Reynard B and Guyot F 1994 High-temperature properties of geikielite ( $\text{MgTiO}_3$ -ilmenite) from high-temperature high-pressure Raman spectroscopy—some implications for  $\text{MgSiO}_3$ -ilmenite *Phys. Chem. Miner.* **21** 441–50
- [74] Chopelas A 1991 Thermal properties of  $\beta\text{-Mg}_2\text{SiO}_4$  at mantle pressures derived from vibrational spectroscopy: implications for the mantle at 400 km depth *J. Geophys. Res.* **96** 11817
- [75] Klotz S, Chervin J-C, Munsch P and Le Marchand G 2009 Hydrostatic limits of 11 pressure transmitting media *J. Phys. D: Appl. Phys.* **42** 75413
- [76] Piermarini G J, Forman R A and Block S 1978 Viscosity measurements in the diamond anvil pressure cell *Rev. Sci. Instrum.* **49** 1061–6
- [77] Hauss  hl S 2007 *Physical Properties of Crystals* ed S Hauss  hl (Weinheim: Wiley)
- [78] Kenichi T 1999 Absence of the *c/a* anomaly in Zn under high pressure with a helium-pressure medium *Phys. Rev. B* **60** 6171–4
- [79] Torikachvili M S, Kim S K, Colombier E, Bud’ko S L and Canfield P C 2015 Solidification and loss of hydrostaticity in liquid media used for pressure measurements *Rev. Sci. Instrum.* **86** 123904
- [80] Syassen K 2008 Ruby under pressure *High Press. Res.* **28** 75–126
- [81] Chai M and Michael Brown J 1996 Effects of static non-hydrostatic stress on the *R* lines of ruby single crystals *Geophys. Res. Lett.* **23** 3539–42
- [82] Piermarini G J, Block S and Barnett J D 1973 Hydrostatic limits in liquids and solids to 100 kbar *J. Appl. Phys.* **44** 5377–82
- [83] Singh A K, Balasingh C, Mao H K, Hemley R J and Shu J 1998 Analysis of lattice strains measured under nonhydrostatic pressure *J. Appl. Phys.* **83** 7567–75